Rafidain Journal of Science
https://rsci.uomosul.edu.iq
Vol. 35, No. 2, pp. 170-181, 2026 (June)

Investigation of Optical and Structural Properties of CuxZn1-xFe2O4 Spinel Thin Films

Laith Sh. Mahmood
Department of Physics/ College of Science/ University of Anbar/ Ramadi/ Iraq

Mazin A. Alalousi
University of Anbar/ Nanomaterials Research Center/ Ramadi/ Iraq

p-ISSN: 1608-9391
e -ISSN: 2664-2786

Article information

Received: 24/6/2025
Revised: 17/8/2025
Accepted: 27/8/2025

DOI: 10.33899/rsci.v35i2.63631

corresponding author:
Laith Sh. Mahmood
lai22s2010@uoanbar.edu.iq
Mazin A. Alalousi
mazin_alalousi@uoanbar.edu.iq

ABSTRACT

This study presents the synthesis and structural characterization of copper-substituted zinc ferrite ($Cu_xZn_{1-x}Fe_2O_4$, x= 0 – 0.09) thin films deposited by electric field enhanced spray pyrolysis—a novel technique for this material system. X-ray diffraction (XRD) investigation demonstrated a cubic spinel structure (space group: Fd-3m) with a preferred (311) orientation in all the compositions. The crystallite size, as estimated from the Williamson-Hall method, varied between 20.92 nm (x = 0) and 66.13 nm (x = 0.09), while the lattice constant decreased from 8.44 Å (x = 0) to 8.30 Å (x = 0.09), indicating compressive strain upon Cu substitution. The cubic spinel phase was also verified using Raman spectroscopy, as it showed the characteristic modes (T^2g, Eg, and A^1g). The A^1g mode shifted from 608.72 cm^{-1} (pure $ZnFe_2O_4$) to 591 cm^{-1} (x = 0.09), suggesting lattice distortion due to Cu incorporation. In addition, the variation in the Copper ion content affects the band gap of $Cu_xZn_{1-x}Fe_2O_4$. The band gap changed between 2.46 eV and 2.92 eV for x= (0 – 0.05). The findings demonstrate that electric field-enhanced spray pyrolysis effectively tunes the structural properties of $Cu_xZn_{1-x}Fe_2O_4$ for potential applications in catalytic and magnetic applications.

Keywords: $Cu_xZn_{1-x}Fe_2O_4$, field-enhanced spray pyrolysis, Raman shift, X-ray density, optical Properties.

INTRODUCTION

Spinel ferrites possess an energy band gap that enables them to absorb light from the visible and ultraviolet regions of the electromagnetic spectrum (Casbeer *et al.,* 2012). Upon absorption, electrons in the material become excited, creating electron-hole pairs. This produces a change in the electrical conductance of the material and forms the principle of their application in photodetectors operating in these spectral regions and even in photocatalytic reactions (Idris *et al.,* 2023). Amongst the spinel ferrites, Cu-Zn ferrites have a tunable band gap (Balaraman *et al.,* 2021).

Such systems, however, are afflicted with a host of problems when applied as photodetectors, including bandgap constraints, charge recombination, Fermi level pinning, and defect density (Ankam *et al.,* 2025) (Liu *et al.,* 2016). Inclusion of functioning under DC bias (Zhu *et al.,* 2022).

Cu-Zn ferrite is a soft magnetic material belonging to the spinel family. Spinel-structured ferrites are among the most widely utilized materials in electrical engineering, primarily due to their favorable magnetic properties (Aman *et al.,* 2022). These ferrites are characterized by high magnetic permeability and electrical resistance, making them particularly suitable for applications in inductors, sensors, low- and high-frequency circuits (Hammad *et al.,* 2018). Moreover, their low eddy current losses further enhance their suitability for use in magnetic and humidity sensors, filter circuits, and transformers (Azam, 2012) (Luo *et al.,* 2021). In addition to their desirable electromagnetic properties, ferrites have compact dimensions, low cost, good stability, and high-quality factor and hence are found to be optimum starting materials for electronic components working at this frequency (Srivastava and Yadav, 2012). The spinel ferrites are crystallized in the AB_2O_4 structure with sites A being occupied by divalent cations such as Ni^{2+}, Zn^{2+}, and Cu^{2+} and sites B being primarily occupied by trivalent cations (Fe^{3+} and Cr^{3+}) (Alahmari *et al.,* 2024). The materials possess a cubic spinel structure with Cu-Zn ferrites exhibiting high magnetic properties (Rathod *et al.,* 2021) (Tatarchuk *et al.,* 2017).

Various synthesis routes have been utilized to synthesize spinel ferrites, including sonochemical, solvothermal (Saleem *et al.,* 2020), co-precipitation (Manzoor *et al.,* 2019), sol-gel auto combustion, hydrothermal (Reena Dhyani *et al.,* 2022), and the Spray Pyrolysis technique (Chaudhari, 2021), The structural and optical properties of spinel ferrites depend mostly on the synthesis route and type and level of dopant employed, where the distribution of cations between A and B sites is an important parameter that determines their physical properties (Reena Dhyani *et al.,* 2022). The spinel as $Cu_xZn_{1-x}Fe_2O_4$ by (Awad and El-Maghraby, 2018) utilizing nitrates as salt in a self-combustion process. As the concentration of copper increases, it was discovered that the particle size grows while the lattice constant (a') drops. (Jamdade *et al.,* 2022), used a green synthesis route via Moringa oleifera extract to prepare copper-doped zinc ferrite nanoparticles, confirming that particle size is a function of Cu^{2+} concentration. (Jamdade *et al.,* 2024) Used the sol-gel auto combustion process, Cu-doped zinc ferrites. They discovered that as the concentration of Cu increases, porosity and lattice parameters fall. The addition of small amounts of copper ions stimulates the crystallization and growth process, which tends to increase the size of the nanocrystals.

The monocrystalline $Cu_xZn_{1-x}Fe_2O_4$ (X=0, 0.3, 0.5, 0.7, and 1) were prepared by (Harisha *et al.,* 2024) via solution combustion technique using Aloe vera gel as the oxide fuel. The lattice parameter was found to decrease with the increase in Cu concentration. It can be observed that the crystal size increases with an increase in Cu content. Furthermore, (Ankam *et al.,* 2025) investigated the influence of copper concentration on structural and optical material behavior of $Cu_xZn_{1-x}Fe_2O_4$ for a range of compositions (x = 0 to 1) UV-Vis spectroscopy revealed peak optical absorption within the 300 - 500 nm range with band gap energies spanning from 1.825 eV to 2.776 eV. Copper doping can influence the crystal structure and optical properties of zinc ferrites

This study aims to synthesize copper-substituted zinc ferrite ($Cu_xZn_{1-x}Fe_2O_4$), where x = 0 to 0.09, and examine its structural properties at room temperature using the electrical field-enhanced spray pyrolysis method. To the best of the authors' knowledge, the application of the electrical field-assisted spray pyrolysis technique for preparing ferrite materials of the formula $Cu_xZn_{1-x}Fe_2O_4$

has not been described elsewhere in the literature. The technique should lead to further preparation of spinel ferrites in more systems, which are becoming increasingly needed for technological and medical applications.

MATERIALS AND METHODS

The following precursors were used: cupric nitrate trihydrate (Cu $(NO_3)_2 \cdot 3H_2O$), zinc acetate (Zn $(CH_3COO)_2$), and ferric nitrate nonahydrate (Fe $(NO_3)_3 \cdot 9H_2O$), that were supplied from Loba Chemie PVT. LTD., Thomas Baker (UK), respectively.

Preparation of solutions

Aqueous precursor solutions were prepared by dissolving ($Cu(NO_3)_2 \cdot 3H_2O$ (2.416 g)(0.1M)), (Zn $(CH_3COO)_2$ (2.195 g) (0.1M)), and Fe $(NO_3)_3 \cdot 9H_2O$ (4.040 g) (0.1M) in 100 mL of deionized water for each. Then were mixed by different ratios as were listed in (Table 1).

Table (1): the ferrite compound solution $Cu_xZn_{1-x}Fe_2O_4$, (x=0 - 0.09)

value (x)	Composition	$Cu(NO_3)_2.3H2O$ (ml)	$((CH_3.COO)_2Zn.2H_2O)$ (ml)	$Fe(NO_3)_3.9H_2O$ (ml)
0	$ZnFe_2O_4$	0	25	25
0.01	$Cu_{0.01}Zn_{0.99}\ Fe_2O_4$	0.25	24.75	25
0.03	$Cu_{0.03}Zn_{0.97}\ Fe_2O_4$	0.75	24.25	25
0.05	$Cu_{0.05}Zn_{0.95}\ Fe_2O_4$	1.25	23.75	25
0.07	$Cu_{0.07}Zn_{0.93}\ Fe_2O_4$	1.75	23.25	25
0.09	$Cu_{0.09}Zn_{0.91}\ Fe_2O_4$	2.25	22.75	25

Synthesis of ferrites

Thin films of $Cu_xZn_{1-x}Fe_2O_4$ were prepared by depositing using the electric field-enhanced spray pyrolysis on N-type silicon substrates with <100> and 1-10 ohm. Cm ($1.5\ cm \times 1.5\ cm$). The optimized substrate temperature is 350±10°C. The deposit process was 15- second spray intervals followed by 15-second pauses. Next, the prepared films were annealed at 500°C for 30 minutes to complete the crystallization process and eliminate defects as much as possible. Fig. (1) illustrates the schematic diagram of the electrical field–enhanced spray pyrolysis technology and its associated equipment. Six thin films of copper-doped zinc ferrite were synthesized according to the value of (x). The reaction is expected to follow the following chemical equation:

$$x\ Cu\ (\ 〖NO〗\_3\ )\_2 \cdot 3H\_2O + (1-x)\ Zn(CH\_3\ COO)\_2 \cdot 2H\_2\ O + 2Fe(NO3)3 \cdot 9H\_2\ O \rightarrow Cu\_x\ Zn\_(1-x)\ Fe\_2\ O\_4\ + (23-2x)\ H\_2\ O + (x+3)\ N\_2 + 2(1-x)\ CO\_2$$

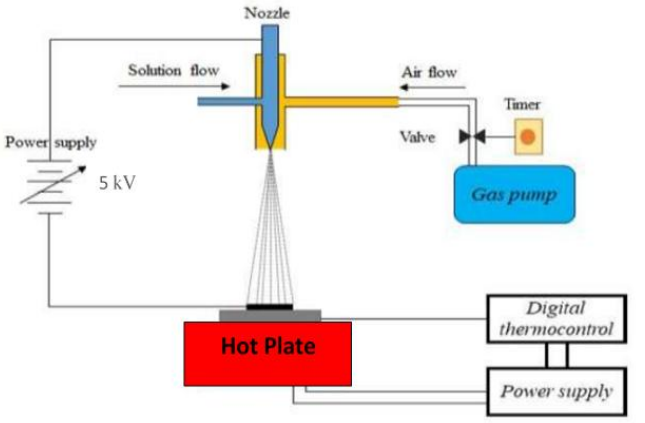

Fig. 1: Schematic diagram of the electrical field–enhanced spray pyrolysis system setup

The structural properties of ferrite were examined by X-ray diffraction (XRD) from Malvern (Aeris compact XRD) at room temperature. The diffraction angle was measured from a 2θ range of 10° to 90° at a scanning velocity of 0.05°/s. Cu-Kα radiation with a wavelength of 1.5405 Å was employed. Addition to Raman shift from 0–900 cm^{-1}, with scan rate of 2.577 cm-1.

RESULT AND DISCUSSION

The XRD patterns shown in Fig. (2) indicate that $Cu_xSZn_{1-x}Fe_2O_4$ films exhibit a polycrystalline structure with a cubic spinel structure. The planes (111), (220), (311), (400), (422), (333), and (440) are represented by peaks at specific angles (2θ) of 18.06°, 29.57°, 34.96°, 42.56°, 52.88 °, 56.44°, and 62.63°. The dominant phase across all prepared samples is 311, related to the $ZnFe_2O_4$ system according to the ICDD 01-082-1049 database. The crystal size was estimated using the Williamson-Hall (W-H) relation and ranged from 16.25 nm to 66.13 nm, as shown in (Table 2), to express the cumulative stress-induced and volumetric stress at the hkl diffraction peak, use equation (1), which is commonly used to account for strain effects that could change the crystallite size value. So, the total stress-induced stress and volume stress at a given peak having an hkl value can be expressed as (1) (Jahil *et al.,* 2022).

$$B_{hkl} = (\beta_{hkl})D_{hkl} + (\beta_{hkl})\,\varepsilon \quad \ldots\ldots\ldots\ldots\ldots\ldots (1)$$

where D_{hkl} (nm) is the crystallite size, β_{hkl} is the full width at half maximum (FWHM) of the diffraction peaks and ε is the strain.

The crystallite size was determined using the Williamson-Hall (W-H) Equation (Mittemeijer and Welzel, 2008) [24](2)

$$cos\ \theta\ \beta_{hkl} = (\frac{A\lambda}{D_{hkl}}) + (4\varepsilon sin\theta) \quad \ldots\ldots\ldots\ldots\ldots\ldots (2)$$

where (A) denotes the dimensionless shape factor (0.9) and θ (rad) is the diffraction angle, increasing the copper ion concentration induces extensive structural growth, including crystallite size and microscopic strain changes as a consequence of site occupation preference and ion redistribution. Cu^{2+} ions preferentially occupy octahedral positions but Zn^{2+} occupies tetrahedral positions (Maria *et al.,* 2013), and increased concentrations lead to Cu^{2+} migration to tetrahedral sites from octahedral sites and generate strain due to incomplete replacement (Khalil and Alalousi, 2024) [26].

This correlation is confirmed by X-ray diffraction data (Table 2), where the shift in diffraction angle increases proportionally to the strain value (Yau, 1988). Exactly, for x=0 (2θ=34.93°), compressive strain (-0.085%) provides 20.92 nm-sized crystallites in an 8.44 Å lattice.

Incorporation of Cu^{2+} (x=0.01, 2θ=35.23°) increases strain (0.159%) and crystallite size (40.83 nm) as Cu^{2+} occupies octahedral sites. Maximum strain (0.135%) at x=0.05 (2θ=34.83°) is synchronized with Zn^{2+} migration into tetrahedral sites (Maria *et al.,* 2013). decreasing crystallites (16.25 nm) and contracting the lattice (8.40 Å). Stable occupancy at x=0.07 (2θ=35.28°) achieves minimum strain (−0.026%) and stability (21.89 nm crystallites). Conversely, Cu dominance at x=0.09 (2θ=35.22°) triggers recrystallization (66.13 nm crystallites), high strain (0.321%), maximum lattice contraction (8.30 Å), and densification (5.588 g/cm³). Interestingly, composite strain is again moderate, suggesting that the material accommodates these site-local redistributions nicely.

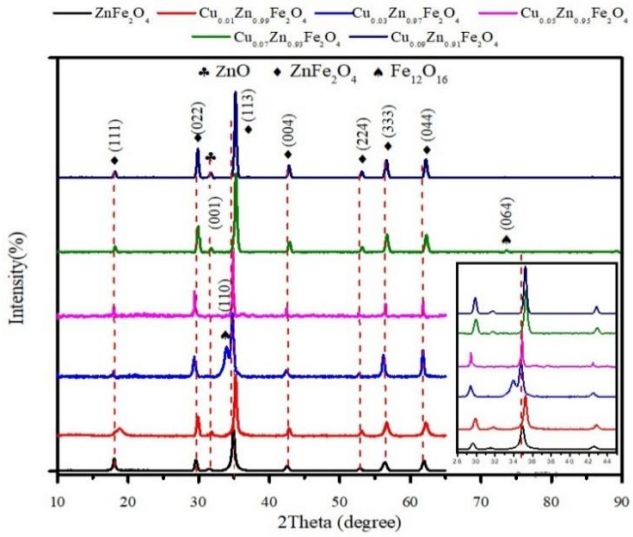

Fig. 2. XRD Diffraction Patterns of $Cu_xZn_{1-x}Fe_2O_4$ (x=0, 0.01, 0.03, 0.05, 0.07, 0.09).

Table (2): XRD data analysis of $Cu_xZn1\text{-}xFe_2O_4$ (x=0, 0.01, 0.03, 0.05, 0.07, 0.09)

x.	[2h.]°	d-spacing[Å]	k l	FWHM [°2T.]	C ryst. Size [nm]	Lattice strain [%]	Lattice constant (Å)	Chemical	Cryst. Syst.	X-ray density (g/cm³)
0	34.93	2.56	311	0.46	20.92	-0.0852	8.44	$ZnFe_2O_4$	Cubic	5.327
0.01	35.23	2.54	311	0.32	40.83	0.159	8.438			5.33
0.03	34.78	2.57	311	0.41	32.04	0.209	8.43			5.35
0.05	34.83	2.57	311	0.61	16.25	0.135	8.40			5.393
0.07	35.28	2.54	311	0.4	21.89	-0.026	8.39			5.418
0.09	35.22	2.54	311	0.36	66.13	0.321	8.30			5.588

The values of the lattice constants for all concentrations (x) of compound $Cu_xZn_{1-x}Fe_2O_4$ were calculated from equation (3) (Bhushan Das *et al.,* 2020).

$$a = \frac{d}{\sqrt{h2+k2+l2}} \quad \ldots\ldots\ldots\ldots\ldots\ldots\ldots \quad (3)$$

where, d = interplanar spacing, a = lattice constant

The lattice constant values, derived from the predominant (311) phase of the X-ray pattern, are presented in (Table 2). The lattice constant diminishes as copper content increases.

While the x-ray densities were estimated using the following formula (Bommannavar *et al*., 2007).

$$d_x = \frac{ZM}{N_A a^3} \ldots\ldots\ldots\ldots\ldots\ldots\ldots\ldots \quad (4)$$

where Z, M, N_A and a^3 are the number of molecules per unit cell, for Cu-Zn ferrite is (Z=8), the molecular weight, Avogadro's number, and volume of the cell, respectively.

In (Table 2), the values of the lattice constants are shown, and we note that pure zinc ferrite has a lattice constant of 8.44 Å, which decreases with increasing copper concentration (Cu^{+2}). Copper ions have a preference for octahedral sites in the structure, while zinc ions have a preference for tetrahedral sites. The decrease in the lattice constant is mainly due to the difference in ionic radius between the substituted ions. Copper ions have a smaller ionic radius (0.72A Å) compared to zinc ions, which have a larger ionic radius (0.83 Å). When Cu^{+2} ions replace Zn^{+2} ions in the spinel lattice, the overall lattice contracts, leading to a decrease in the lattice constant (Nadhiya *et al.,* 2023). As the amount of copper contained increases, the lattice constant decreases, increasing the X-ray density.

The increased density of Cu^{+2} ions (8.92 g/cm³) in comparison with Zn^{+2} ions (7.14 g/cm³) cause the density of X-rays to increase when Cu^{+2} is added (Abu-Elsaad and A. S. Nawara,2024).

Raman spectroscopy is a very useful way to study the small details, arrangement, disorder, changes, and stress in a material by looking at changes in its polarization. Fig. (3) shows the Raman spectra of copper-substituted zinc ferrite nanofilms obtained at room temperature in the range of 100–800 cm^{-1}. All recorded Raman spectra are compatible with a cubic spinel structure, exhibiting excellent structural stability even when doped with copper, with no phase shift seen. The substitution of zinc for copper led to minor alterations in the intensity and frequency of the principal Raman active modes. Group theory states that ten Raman modes ($2A_{1g} + 3B_{1g} + B_{2g} + 4E_g$) belong to tetragonal spinel structure, while five Raman modes ($A_{1g} + E_g + 3T_{2g}$) correspond to cubic spinel structure (Reena Dhyani *et al*.2022). The formula for the Raman modes of cubic-structured materials is $U = A_{1g} + E_g + 3T_{2g}$. Normally, we detect three first-order Raman active modes: $A_{1g} + E_g + T_{2g}$. The A_{1g} mode is characterized by the symmetric stretching of oxygen atoms along Fe-O bonds, whereas the E_g mode is too symmetric. Asymmetric stretching of iron is the result of oxygen bending with regard to iron ions and T_{2g} mode. The symbols used, like A for a one-dimensional mode and E and T for two-dimensional modes, are modes of Raman in three dimensions. Together with this, the subscript the symbol for symmetry with regard to the center of inversion is g (Tandon *et al.,* 2020).

In spinel ferrites, the vibrations of (Mtet–O) at the tetrahedral sites cause the higher wavenumber Raman modes above 600–720 cm−1, while the vibrations of (Moct–O) at the octahedral sites cause the lower wavenumber modes in the range of 460–660 cm−1.Three very intense peaks, namely A_{1g}, T_{2g} (3), and T_{2g} (2), dominate the Raman spectrum. The mode A_{1g} is located between 570 and 780 cm^{-1}, the T_{2g} (3) mode at about 450-500 cm^{-1}, and the T_{2g} (2) mode at about 350-400 cm^{-1}. The two low-frequency modes, T2g (1) and E_g, are found at frequencies below 300 cm^{-1} (Albini *et al.,* 2023). A_{1g} shows how oxygen atoms stretch evenly along the Fe-O bonds, T2g shows uneven stretching of iron, and E_g shows how oxygen bends evenly in relation to iron ions. (Table 3) displays the related modes, The peak position decreases from about 609 cm^{-1} in pure $ZnFe_2O_4$ to about 591 cm^{-1} at x = 0.09. This shift indicates that substituting Zn with Cu in the spinel ferrite tends to soften or slightly weaken the symmetric stretching vibrations of oxygen atoms along the Fe-O bonds in the tetrahedral sites. This trend is typical in doped spinel ferrites, were cation substitution changes vibrational modes. The spectra are predominantly characterized by the A_{1g} mode. This mode is linked to the symmetric breathing vibration of the tetrahedral AO4 unit, with the cation positioned in the center of a cube, encircled by four oxygen atoms located at the non-adjacent corners (Hosterman,2011).

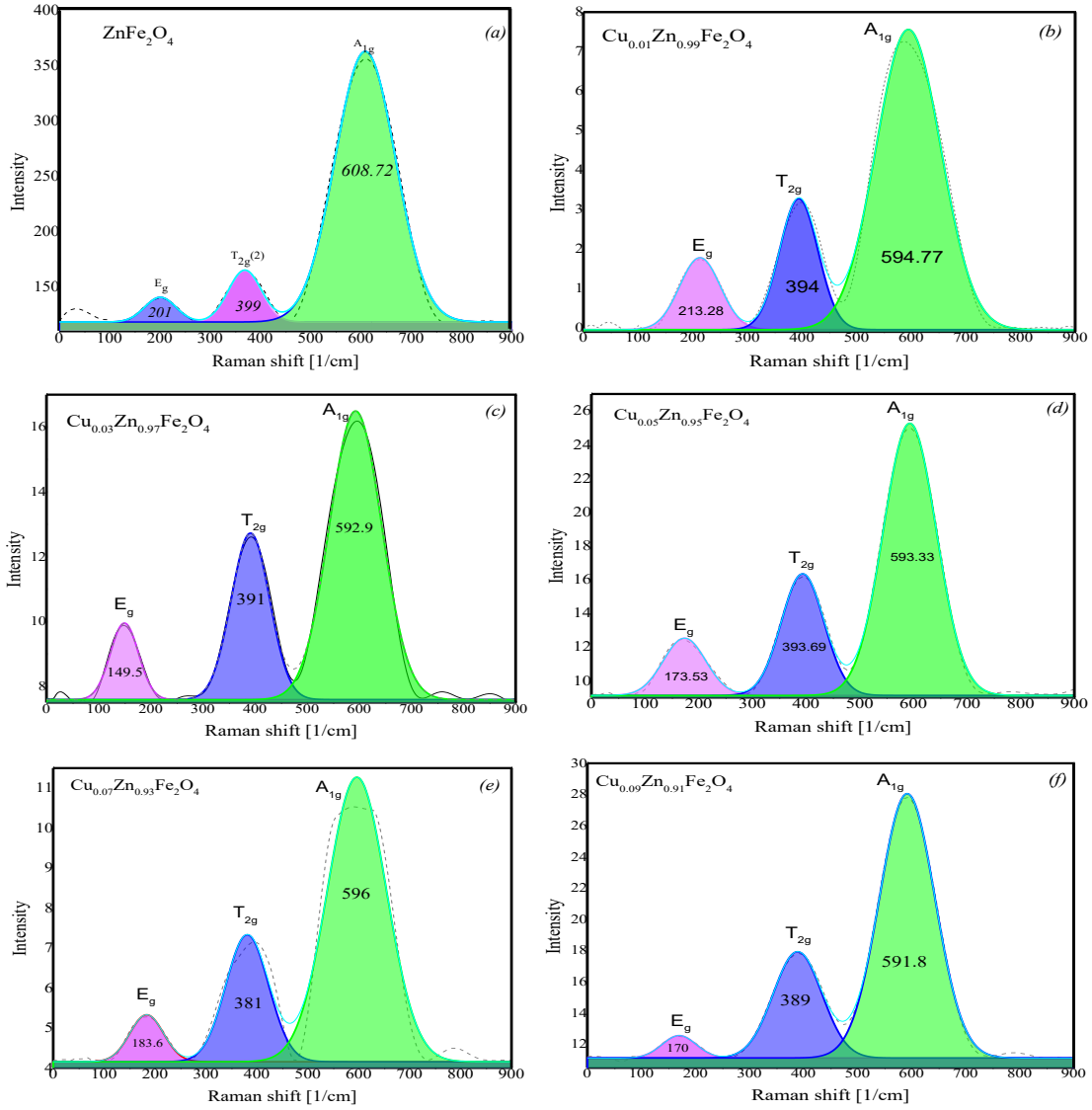

Fig. 3: (a-f) Raman spectra of $Cu_xZn_{1-x}Fe_2O_4$ ferrite (x=0,0.01,0.03,0.05,0.07,0.09)

Table (3): Raman active modes of CuxZn1-xFe2O4 ferrite (x=0,0.01,0.03,0.05,0.07,0.09)

Sample Name	A_{1g} (cm^{-1})	E_g (cm^{-1})	T_{2g} (cm^{-1})
$ZnFe_2O_4$	608.72	201	399
$Cu_{0.01}Zn_{0.99}Fe_2O_4$	594.77	213.28	394
$Cu_{0.03}Zn_{0.97}Fe_2O_4$	592.9	149.5	391
$Cu_{0.05}Zn_{0.95}Fe_2O_4$	593.33	173.53	393.69
$Cu_{0.07}Zn_{0.93}Fe_2O_4$	596	183.6	381
$Cu_{0.09}Zn_{0.91}Fe_2O_4$	591	170	389

The energy band gap (E_g) is an important parameter for its use in various optoelectronic devices. It decides the wavelength of light that could be absorbed by the material (Tasleem *et al.,* 201 9). UV and visible spectra of samples ($Cu_xZn_{1-x}Fe_2O_4$) were obtained at room temperature for x values (0, 0.01, 0.03, 0.05, 0.07, 0.09) over the wavelength range of 200–800 nm. Pure zinc ferrite ($ZnFe_2O_4$) was found to be absorbing ultraviolet and visible light in the range of 284 to 496 nm, while copper-doped zinc ferrite was showing its highest absorption in the ultraviolet range of 297 to 420 nm, as seen in Fig. (4). The energy of the optical gap can be determined by the application of the Tauc equation ($\alpha h\upsilon = B\ (h\upsilon - E_g)^n$). Plot at $(\alpha h\upsilon)^2$ vs $h\upsilon$ is shown in Fig. (5). The values of the band gap for (x=0-0.09) are 2.46 eV, 2.54 eV, 2.55 eV, 2.92 eV, 2.28 eV, and 2.5 eV, respectively. The optical band gap value was found to be greater with higher concentration of copper in the zinc ferrite system by virtue of a blue shift due to a change in the wavelength of the absorption towards the shorter wavelengths. This is caused by introducing additional energy levels inside the sub-band gap because of the high concentration of surface and interface defects introduced in the aggregated particles (Anand *et al.,* 2014).

Above x = 0.05, the band gap decreases primarily due to increased lattice strain, leading to structural disorder and defect states within the material. With an increase in the doping level, the lattice strain increases (from 0.135% at x=0.05 to 0.312% at x=0.09). This greater doping perturbs the crystal structure, leading to localized defect state formation, which essentially reduces the band gap. Heavy doping has also been found to produce band gap narrowing via the creation of extra energy levels and increased carrier concentration (Kawamura *et al.,* 2023), adding to the reduced band gap energy observed above x=0.05 There are a number of factors that affect the energy gap values, which are the film-forming process, the preparation method, the conditions in which the process of preparation is carried out, the nature of the crystal structure, and the distribution of atoms in the crystal lattice (Anyaegbunam and C. Augustine,2018). The compound can be used by optoelectronic devices and photocatalysis due to its band gap energies.

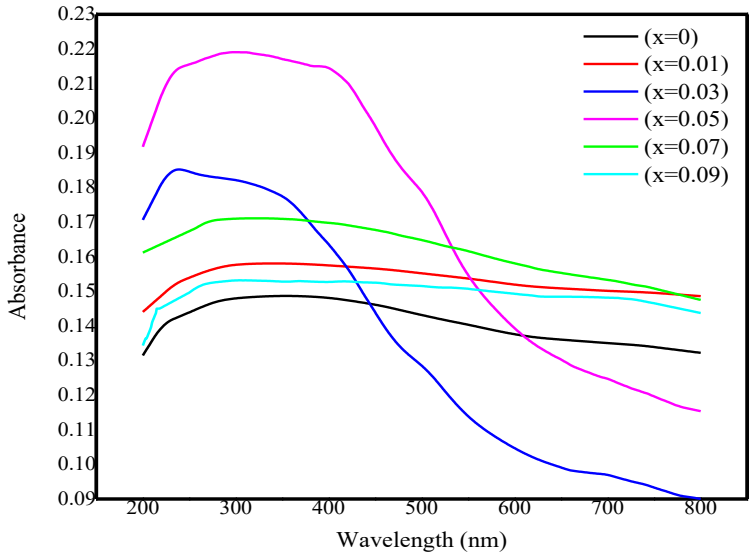

Fig. 4. The optical absorbance of the copper-doped zinc ferrite films $Cu_xZn_{(1-x)}Fe_2O_4$

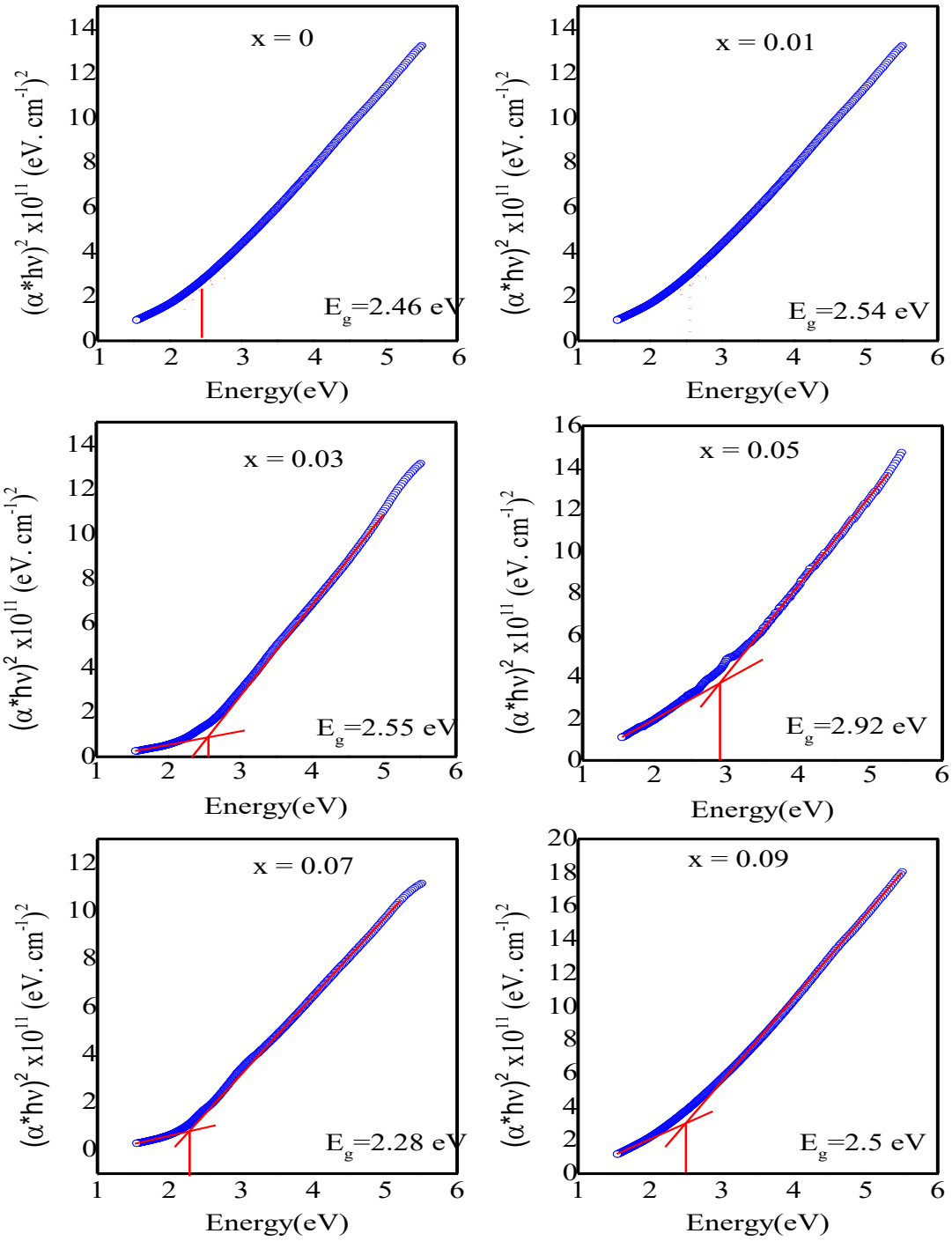

Fig. 5. The optical Band gap of the copper-doped zinc ferrite films $Cu_xZn_{(1-x)}Fe_2O_4$

CONCLUSIONS

Copper-substituted zinc ferrite ($Cu_xZn_{1-x}Fe_2O_4$, x = 0 – 0.09) thin films have been deposited using electric field-enhanced spray pyrolysis, a novel and successful technique for depositing this cubic-structured material system. Though minor ionic additions do not change the crystal structure stages of the as-synthesized Cu^{2+} ferrite, they induce compressive stresses via Cu^{2+} substitution and crystal growth, significantly affecting the optical and, maybe, magnetic properties. This technique has been shown to be an easy and inexpensive technique for depositing high-quality thin films with engineered structural properties. This ability to design the structural and microstructural properties of $Cu_xZn_{1-x}Fe_2O_4$ thin films makes them suitable for catalytic, magnetic, and electronic devices requiring stringent control over crystal lattice stress and crystallization.

REFERENCES

Abu-Elsaad, N.I.; Nawara, A.S. (2024). Effect of Cu substitution on magnetic and photocatalytic properties of Mn–ZnFe2O4 nanoparticles. *J. Mater. Sci.* [Internet]. **59**(10), 4167–85. DOI:org/10.1007/s10853-024-09486-8

Alahmari, F.; Khan, F.A.; Sozeri, H.; Sertkol, M.; Jaremko, M. (2024). Structure , optical and magnetic properties , and. 7540–7550.

Albini, B.; Restelli, S.; Ambrosetti, M.; Bini, M.; D'Amico, F.; Mozzati, M. C. (2023). Raman spectroscopy in pure and doped zinc ferrites nanoparticles. *J. Mater. Sci*. **34**(12), 1–10. DOI: org/10.1007/s10854-023-10464-0

Aman, S.; Ahmad, N.; Alhossainy, M. H.; Albalawi, H.; Morsi, M.; Al-Muhimeed, T. I. (2022). Structural, magnetic, electrical and microwave properties of spinel ferrites. *J. Rare. Earths.* **40**(3), 443–50. Available from. DOI.org/10.1016/j.jre.2021.04.015

Anand, G. T.; Kennedy, L. J.; Vijaya, J. J.; Kaviyarasan, K.; Sukumar, M. (2014). Structural, optical and magnetic characterization of Zn1−xNixAl2O4 ($0 \leq x \leq 5$) spinel nanostructures synthesized by microwave combustion technique. *Ceram. Int.*, **40**(9), 14135–46. Available from. DOI.org/10.1016/j.ceramint.2014.05.150

Ankam, V.; Karka, G.; Reddy, L. G. (2025). Structural and Optical Properties of Copper-Doped Zinc Ferrites Using Solid State Reaction Method. *J. Nano. Electron. Phys.*, **7**(1), 1–13. DOI.org/10.21272/jnep.**7**(1).01001

Anyaegbunam, F. N. C.; Augustine, C. (2018). A Study of Optical Band Gap and Associated Urbach Energy Tail of Chemically Deposited Metal Oxides Binary Thin Films. *Dig. J. Nanom. Biostrt.* **13**(3), 847–56.

Awad, H. M.; El-Maghraby, A. (2018). Preparation, structure and catalytic activity of simple spinel as nano-copper-zinc ferrites in industry model. *Rasayan. J. Chem.* **11**(3), 1320–7. DOI.org/10.31788/RJC.2018.1134015

Azam, A. (2012). Microwave assisted synthesis and characterization of Co doped Cu ferrite nanoparticles. *J. Alloys. Compd.*, **540**:145–53. DOI.org/10.1016/j.jallcom.2012.06.068

Bhushan Das, S.; Kumar Singh, R.; Kumar, V.; Kumar, N.; Kumar, S. (2020). Tailoring the structural, optical and multiferroic properties of low temperature synthesized cobalt ferrite nanomaterials, by citrate precursor method. *Mater. Today. Proc.*, **46**, 6527–33. DOI.org/10.1016/j.matpr.2021.04.001

Bommannavar, B. K.; Kulkarni, P. P.; Bote, V. R.; Naik, L. R.; Pujar, R. B. (2007). Effect of sintering temperature and time on resistivity and microstructure of CuxCo1-xFe2O4 ferrites. *Bull. Mater. Sci.*, **6**(4), 2–7.

Casbeer, E.; Sharma, V. K.; Li, X. Z. (2012). Synthesis and photocatalytic activity of ferrites under visible light: A review. *Sep. Purif. Technol.* **87**, 1–14. DOI.org/10.1016/j.seppur.2011.11.034

Chaudhari, M. N. (2021). Thin film Deposition Methods: A Critical Review. *Int. J. Res. Appl. Sci. Eng. Technol.,* **9**(6), 5215–32. DOI.org/10.22214/ijraset.2021.35626

Dhyani, R.; Srivastava, R. C.; Rawat, P. S.; Dixit, G. (2022). Structural and elastic properties of tetragonal nano-structured copper ferrite. *Int. J. Mater. Res.,* **113**:884–92. DOI.org/10.1515/ijmr-2021-8406

Hammad, T. M.; Salem, J. K.; Amsha, A. A.; Hejazy, N. K. (2018). Optical and magnetic characterizations of zinc substituted copper ferrite synthesized by a co-precipitation chemical method. *J. Alloys. Compd.*, **741**:123–30. DOI.org/10.1016/j.jallcom.2018.01.127

Harisha, G.; Thejas, R.; Padmini, B. V.; et al. (2024). Structural, morphological, magnetic, and dielectric properties of copper-substituted CuXZn(1-X)Fe2O4 nanoparticles: Green synthesis. *J. Met. Mater. Miner.,* **34**(3), 1–7. DOI.org/10.55713/jmmm.v34i3.1895

Idris, M. G.; Hafeez, H. Y.; Mohammed, J.; et al. (2023). A review on recent development in the spinel ferrites-based materials for efficient solar fuel (hydrogen) generation via photocatalytic water-splitting. *Appl. Surf. Sci. Adv.*, **18**, 100468.

DOI.org/10.1016/j.apsadv.2023.100468

Jahil, S. S.; Mohammed, I. A.; Khazaal, A. R.; Jasim, K. A.; Harbbi, K. H. (2022). Application the Halder–Wagner to Calculation Crystal Size and Micro Strain by X-ray Diffraction Peaks Analysis. *NeuroQuant.*, **20**(1), 199–204. DOI.org/10.14704/nq.2022.20.1.NQ22021

Jamdade, S.; Tambade, P.; Rathod, S. (2024). Study of Variation in Porosity and Its Associated Parameters Due To Cu Doping in Zinc Ferrite Using Sol-Gel Auto-Combustion Method. *UPB. Sci. Bull. Ser. B. Chem. Mater. Sci.,* **86**(1), 227–34.

Liu, Y.; Hsu, J.; Fu, Y.; Tsai, K. (2016). Preparation of Cu-Zn ferrite photocatalyst and its application. *Int. J. Hydrogen. Energy.* **41**(38), 1–7. DOI.org/10.1016/j.ijhydene.2016.04.127

Luo, F.; Duan, Z.; Zhang, Y.; Shang, Y. (2021). Influence of microstructure optimization on magnetic and thermal properties of MnZn ferrite. *J. Mater. Sci. Mater. Electron.* **32**(12), 15633–42. DOI.org/10.1007/s10854-021-06112-0

Manzoor, T.; Javed, T.; Mustafa, G.; et al. (2019). Facile synthesis of CuxZn1−xFe2O4 nanoparticles and their thermo-physical properties evaluation. *Appl. Phys. A. Mater. Sci. Process.,* **125**(9), 619. DOI.org/10.1007/s00339-019-2917-x

Maria, K. H.; Choudhury, S.; Hakim, M. A. (2013). Structural phase transformation and hysteresis behavior of Cu-Zn ferrites. *Int. Nano. Lett.*, **3**(1), 1–10. DOI.org/10.1186/2228-5326-3-42

Nadhiya, D.; Kala, A.; Sasikumar, P.; et al. (2023). Influence of Cu2+ substitution on the structural, optical, magnetic, and antibacterial behaviour of zinc ferrite nanoparticles. *J. Saudi. Chem. Soc.,* **27**(5), 101696. DOI.org/10.1016/j.jscs.2023.101696

Rathod, S. M.; Chavan, A. R.; Jadhav, S. S.; et al. (2021). Ag+ ion substituted CuFe2O4 nanoparticles: Analysis of structural and magnetic behavior. *Chem. Phys. Lett.,* **765**, 138318. DOI.org/10.1016/j.cplett.2020.138318

Saleem, A.; Zhang, Y.; Gong, H.; et al. (2020). Electromagnetic wave absorption performance of Ni doped Cu-ferrite nanocrystals. *Mater. Res. Express.,* **7**(1), 016117. DOI.org/10.1088/2053-1591/ab68ba

Tandon, V.; Saleem, M.; Kaurav, N.; Dixit, R. C. (2020). Influence of barium (Ba2+) doping for Cu-Zn ferrites on structural and electrical properties. *Mater. Today. Proc.,* **30**, 234–7. DOI.org/10.1016/j.matpr.2020.06.520

Tasleem, M.; Hashim, M.; Naidu, K. C. B.; et al. (2019). Optical and electronic properties of copper and cobalt substituted nano SrBaFe12O19 synthesized by sol–gel autocombustion method. *Appl. Phys. A. Mater. Sci. Process.,* **125**(5), 329. DOI.org/10.1007/s00339-019-2618-5

Tatarchuk, T.; Bououdina, M.; Macyk, W.; et al. (2017). Structural, Optical, and Magnetic Properties of Zn-Doped CoFe2O4 Nanoparticles. *Nanoscale. Res. Lett.,* **12**(1), 141. DOI.org/10.1186/s11671-017-1903-y

Yadav, K.; Ahmed, G.; Chauhan, H. (2022). GREEN SYNTHESIS OF Cu-DOPED ZINC NANO FERRITE MATERIALS USING Moringa Oleifera LEAVES. *J. Indian. Res.,* **10**(57).

Yau, J. K. (1988). Evaluation of crystallite size and strain from X-ray diffraction pattern. *Thesis/Tech. Rep.* **1988**.

Zhu, J.; Zhu, Y.; Chen, Z.; Wu, S.; Fang, X.; Yao, Y. (2022). Progress in the Preparation and Modification of Zinc Ferrites Used for the Photocatalytic Degradation of Organic Pollutants. *Molecules*., **27**(16), 5151. DOI.org/10.3390/molecules27165151

دراسة الخواص البصرية والبنيوية لأغشية السبينيل الرقيقة $Cu_xZn_{1-x}Fe_2O_4$

ليث شاكر محمود

قسم الفيزياء/ كلية العلوم/ جامعة الانبار/ الرمادي / العراق.

مازن عبد الحميد الالوسي

جامعة الانبار/ مركز بحوث المواد النانوية / رمادي / العراق.

الملخص

تقدم هذه الدراسة تخليق وتوصيف هيكلي لأغشية رقيقة من فيريت الزنك ($Cu_xZn_{1-x}Fe_2O_4$، $x=0 - 0.09$) مُستبدلة بالنحاس، مُرسبة بتقنية التحلل الحراري بالرش المُعزز بالمجال الكهربائي، وهي تقنية جديدة لهذا النظام المادي. أظهر فحص حيود الأشعة السينية (XRD) بنية سبينيل مكعبة (المجموعة الفراغية: Fd-3m ذات اتجاه مفضل (311) في جميع التركيبات. تراوح حجم البلورة، المُقدر بطريقة ويليامسون–هول، بين 20.92 نانومتر ($x=0$) و66.13 نانومتر ($x=0.09$)، بينما انخفض ثابت الشبكة من 8.44 Å ($x=0$) إلى 8.30 Å ($x=0.09$)، مما يدل على إجهاد انضغاطي عند استبدال النحاس. تم التحقق من طور السبينيل المكعب باستخدام مطيافية رامان، حيث أظهر الأنماط المميزة (T_{2g}، E_g، A_{1g}). تحول نمط A_{1g} من 608.72 سم$^{-1}$ ($ZnFe_2O_4$ نقي) إلى 591 سم$^{-1}$ ($x = 0.09$) ، مما يشير إلى تشوه الشبكة بسبب إضافة النحاس. بالإضافة إلى ذلك، يؤثر التباين في محتوى أيونات النحاس على فجوة النطاق لـ $Cu_xZn_{1-x}Fe_2O_4$. تراوحت فجوة النطاق بين 2.46 إلكترون فولت و2.92 إلكترون فولت عند ($x = 0 – 0.05$). تُظهر النتائج أن التحلل الحراري بالرش المُحسَّن بالمجال الكهربائي يُحسّن بفعالية الخصائص الهيكلية لـ $Cu_xZn_{1-x}Fe_2O_4$ للتطبيقات المحتملة في التطبيقات الحفزية والمغناطيسية.

الكلمات الدالة: $Cu_xZn_{1-x}Fe_2O_4$، التحلل الحراري بالرش المعزز بالمجال، انزياح رامان، كثافة الأشعة السينية، الخصائص البصرية.